
Autodecoding Latent 3D Diffusion Models

Evangelos Ntavelis* Computer Vision Lab ETH Zurich Zürich, Switzerland entavelis@vision.ee.ethz.ch	Aliaksandr Siarohin Creative Vision Snap Inc. Santa Monica, CA, USA asiarohin@snapchat.com	Kyle Olszewski Creative Vision Snap Inc. Santa Monica, CA, USA kolszewski@snap.com
---	---	---

Chaoyang Wang CI2CV Lab Carnegie Mellon University Pittsburgh, PA, USA chaoyanw@cs.cmu.edu	Luc Van Gool CVL, ETH Zurich, CH PSI, KU Leuven, BE INSAIT, Un. Sofia, BU vangool@vision.ee.ethz.ch	Sergey Tulyakov Creative Vision Snap Inc. Santa Monica, CA, USA stulyakov@snapchat.com
---	--	---

Abstract

We present a novel approach to the generation of static and articulated 3D assets that has a 3D *autodecoder* at its core. The 3D *autodecoder* framework embeds properties learned from the target dataset in the latent space, which can then be decoded into a volumetric representation for rendering view-consistent appearance and geometry. We then identify the appropriate intermediate volumetric latent space, and introduce robust normalization and de-normalization operations to learn a 3D diffusion from 2D images or monocular videos of rigid or articulated objects. Our approach is flexible enough to use either existing camera supervision or no camera information at all – instead efficiently learning it during training. Our evaluations demonstrate that our generation results outperform state-of-the-art alternatives on various benchmark datasets and metrics, including multi-view image datasets of synthetic objects, real in-the-wild videos of moving people, and a large-scale, real video dataset of static objects.

Code & Visualizations: <https://github.com/snap-research/3DVADER>

1 Introduction

Photorealistic generation is undergoing a period that future scholars may well compare to the enlightenment era. The improvements in quality, composition, stylization, resolution, scale, and manipulation capabilities of images were unimaginable just over a year ago. The abundance of online images, often enriched with text, labels, tags, and sometimes per-pixel segmentation, has significantly accelerated such progress. The emergence and development of denoising diffusion probabilistic models (DDPMs) [68, 70, 24] propelled these advances in image synthesis [49, 71, 73, 69, 15, 16, 59, 32, 79] and other domains, *e.g.* audio ([8, 18, 88]) and video ([20, 82, 75, 25, 21, 43]).

However, the world is 3D, consisting of static and dynamic objects. Its geometric and temporal nature poses a major challenge for generative methods. First of all, the data we have consists mainly of images and monocular videos. For some limited categories of objects, we have 3D meshes with corresponding multi-view images or videos, often obtained using a tedious capturing process or created manually by artists. Second, unlike CNNs, there is no widely accepted 3D or 4D representation suitable for 3D geometry and appearance generation. As a result, with only a few exceptions [67], most of the existing 3D generative methods are restricted to a narrow range of object

*Work done during internship at Creative Vision Team - Snap Inc

categories, suitable to the available data and common geometric representations. Moving, articulated objects, *e.g.* humans, compound the problem, as the representation must also support deformations.

In this paper, we present a novel approach to designing and training denoising diffusion models for 3D-aware content suitable for efficient usage with datasets of various scales. It is generic enough to handle both rigid and articulated objects. It is versatile enough to learn diverse 3D geometry and appearance from multi-view images and monocular videos of both static and dynamic objects. Recognizing the poses of objects in such data has proven to be crucial to learning useful 3D representations [5, 6, 66, 67]. Our approach is thus designed to be robust to the use of ground-truth poses, those estimated using structure-from-motion, or using no input pose information at all, but rather learning it effectively during training. It is scalable enough to train on single- or multi-category datasets of large numbers of diverse objects suitable for synthesizing a wide range of realistic content.

Recent diffusion methods consist of two stages [59]. During the first stage, an autoencoder learns a rich latent space. To generate new samples, a diffusion process is trained during the second stage to explore this latent space. To train an image-to-image autoencoder, many images are needed. Similarly, training 3D autoencoders requires large quantities of 3D data, which is very scarce. Previous works used synthetic datasets such as ShapeNet [7] (DiffRF[45], SDFusion [10], *etc.*), and were thus restricted to domains where such data is available.

In contrast to these works, we propose to use a volumetric *autodecoder* to learn the latent space for diffusion sampling. In contrast to the autoencoder-based approach, our autodecoder maps a 1D vector to each object in the training set, and thus does not require 3D supervision. The autodecoder learns 3D representations from 2D observations, using rendering consistency as supervision. Following UVA [63] this 3D representation supports the articulated parts necessary to model non-rigid objects.

There are several key challenges with learning such a rich, latent 3D space with an autodecoder. First, our autodecoders do not have a clear “bottleneck.” Starting with a 1D embedding, they upsample it to latent features at many resolutions, until finally reaching the output radiance and density volumes. Here, each intermediate volumetric representation could potentially serve as a “bottleneck.” Second, autoencoder-based methods typically regularize the bottleneck by imposing a KL-Divergence constraint [34, 59], meaning diffusion must be performed in this regularized space.

To identify the best scale, one can perform exhaustive layer-by-layer search. This, however, is very computationally expensive, as it requires running hundreds of computationally expensive experiments. Instead, we propose robust normalization and denormalization operations which can be applied to any layers of a pre-trained and fixed autodecoder. These operations compute robust statistics to perform layer normalization and, thus, allow us to train the diffusion process at any intermediate resolution of the autodecoder. We find that at fairly low resolutions, the space is compact and provides the necessary regularization for geometry, allowing the training data to contain only sparse observations of each object. The deeper layers, on the other hand, operate more as upsamplers. We provide extensive analysis to find the appropriate resolution for our autodecoder-based diffusion techniques.

We demonstrate the versatility and scalability of our approach on various tasks involving rigid and articulated 3D object synthesis. We first train our model using multi-view images and cameras in a setting similar to DiffRF [45] to generate shapes of a limited number of object categories. We then scale our model to hundreds of thousands of diverse objects train using the real-world MVIImgNet [85] dataset, which is beyond the capacity of prior 3D diffusion methods. Finally, we train our model on a subset of CelebV-Text [83], consisting of $\sim 44\text{K}$ sequences of high-quality videos of human motion.

2 Related Work

2.1 Neural Rendering for 3D Generation

Neural radiance fields, or NeRFs (Mildenhall et al., 2020 [44]), enable high-quality novel view synthesis (NVS) of rigid scenes learned from 2D images. Its approach to volumetric neural rendering has been successfully applied to various tasks, including *generating* objects suitable for 3D-aware NVS. Inspired by the rapid development of generative adversarial models (GANs) [19] for generating 2D images [19, 4, 28, 29, 31, 30] and videos [72, 65, 84], subsequent work extends them to 3D content generation with neural rendering techniques. Such works [61, 47, 50, 48, 81] show promising results for this task, yet suffer from limited multi-view consistency from arbitrary viewpoints, and experiencing difficulty in generalizing to multi-category image datasets.

A notable work in this area is pi-GAN (Chan et al., 2021 [5]), which employs neural rendering with periodic activation functions for generation with view-consistent rendering. However, it requires a precise estimate of the dataset camera pose distribution, limiting its suitability for free-viewpoint videos. In subsequent works, EG3D (Chan et al., 2022 [6]) and EpiGRAF (Skorokhodov et al. [66]) use tri-plane representations of 3D scenes created by a generator-discriminator framework based on StyleGAN2 (Karras et al., 2020 [31]). However, these works require pose estimation from keypoints (e.g. facial features) for training, again limiting the viewpoint range.

These works primarily generate content within one object category with limited variation in shape and appearance. A notable exception is 3DGP [67], which generalizes to ImageNet [13]. However, its reliance on monocular depth prediction limits it to generating front-facing scenes. These limitations also prevent these approaches from addressing deformable, articulated objects. In contrast, our method is applicable to both deformable and rigid objects, and covers a wider range of viewpoints.

2.2 Denoising Diffusion Modeling

Denoising diffusion probabilistic models (DDPMs) [68, 24] represent the generation process as the learned denoising of data progressively corrupted by a sequence of diffusion steps. Subsequent works improving the training objectives, architecture, and sampling process [24, 15, 79, 32, 59, 49, 69] demonstrated rapid advances in high-quality data generation on various data domains. However, such works have primarily shown results for tasks in which samples from the target domain are fully observable, rather than operating in those with only partial observations of the dataset content.

One of the most important of such domains is 3D data, which is primarily observed in 2D images for most real-world content. Some recent works have shown promising initial results in this area. DiffRF [45] proposes reconstructing per-object NeRF volumes for synthetic datasets, then applying diffusion training on them within a U-Net framework. However, it requires the reconstruction of many object volumes, and is limited to low-resolution volumes due to the diffusion training’s high computational cost. As our framework instead operates in the latent space of the autoencoder, it effectively shares the learned knowledge from all training data, thus enabling low-resolution, latent 3D diffusion. In [10], a 3D autoencoder is used for generating 3D shapes, but this method requires ground-truth 3D supervision, and only focuses on shape generation, with textures added using an off-the-shelf method [56]. In contrast, our framework learns to generate the surface appearance and corresponding geometry without such ground-truth 3D supervision. Recently, several works [56, 39, 9] propose using large-scale, pre-trained text-to-image 2D diffusion models for 3D generation. The key idea behind these methods is to use 2D diffusion models to evaluate the quality of renderings from randomly sampled viewpoints, then use this information to optimize a 3D-aware representation of the content. Compared to our method, however, such approaches require a far more expensive optimization process to generate each novel object.

3 Methodology

Our method is a two-stage approach. In the first stage, we learn an autoencoder G containing a library of embedding vectors corresponding to the objects in the training dataset. These vectors are first processed to create a low-resolution, latent 3D feature volume, which is then progressively upsampled and finally decoded into a voxelized representation of the generated object’s shape and appearance. This network is trained using volumetric rendering techniques on this volume, with 2D reconstruction supervision from the training images.

During the second stage, we split the autoencoder G into two parts, $G = G_2 \circ G_1$. We then employ this autoencoder to train a 3D diffusion model operating in the compact, 3D latent space obtained from G_1 .² Using the structure and appearance properties extracted from the autoencoder training dataset, this 3D diffusion process allows us to use this network to efficiently generate diverse and realistic 3D content. The full pipeline is depicted in Fig. 1.

Below, we first describe the volumetric autoencoding architecture (Sec. 3.1). We then describe the training procedure and reconstruction losses for the autoencoder (Sec. 3.2). Finally, we provide details for our training and sampling strategies for 3D diffusion in the decoder’s latent space (Sec. 3.3).

²We experimented with diffusion at different feature volume resolutions, ranging from 4^3 at the earliest stage to 16^3 in the later stages. These results are described in our evaluations (Sec. 4.3, Fig. 3).

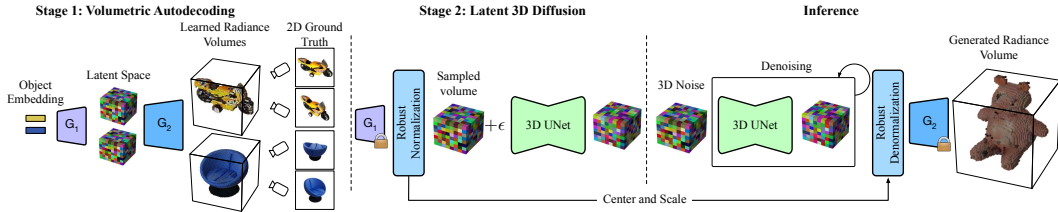


Figure 1: **Our proposed two-stage framework.** Stage 1 trains an autodecoder with two generative components, G_1 and G_2 . It learns to assign each training set object a 1D embedding that is processed by G_1 into a latent volumetric space. G_2 decodes these volumes into larger radiance volumes suitable for rendering. Note that we are using only 2D supervision to train the autodecoder. In Stage 2, the autodecoder parameters are frozen. Latent volumes generated by G_1 are then used to train the 3D denoising diffusion process. At inference time, G_1 is not used, as the generated volume is randomly sampled, denoised, and then decoded by G_2 for rendering.

3.1 Autodecoder architecture

Canonical Representation. We use a 3D voxel grid to represent the 3D structure and appearance of an object. We assume the objects are in their canonical pose, such that the 3D representation is decoupled from the camera poses. This decoupling is necessary for learning compact representations of objects, and also serves as a necessary constraint to learn meaningful 3D structure from 2D images without direct 3D supervision. Specifically, the canonical voxel representation consists of a density grid $V^{\text{Density}} \in \mathbb{R}^{S^3}$ which is a discrete representation of the density field with resolution S^3 , and $V^{\text{RGB}} \in \mathbb{R}^{S^3 \times 3}$ which represents the RGB radiance field. We employ volumetric rendering, integrating the radiance and opacity values along each view ray similar to NeRFs [44]. In contrast to the original NeRF, however, rather than computing these local values using an MLP, we tri-linearly interpolate the density and RGB values from the decoded voxel grids.

Voxel Decoder. The 3D voxel grids for density and radiance, V^{Density} and V^{RGB} , are generated by a volumetric autodecoder G that is trained using rendering supervision from 2D images. We choose to directly generate V^{Density} and V^{RGB} , rather than intermediate representations such as feature volumes or tri-planes, as it is more efficient to render and ensures consistency across multiple views. Note that feature volumes and tri-planes require running an MLP pass for each sampled point, which requires significant computational cost and memory during training and inference.

The decoder is learned in the manner of GLO [3] across various object categories from large-scale multi-view or monocular video datasets. The architecture of our autodecoder is adapted from that used in [63]. However, in our framework we want to support large scale datasets which poses a challenge in designing the decoder architecture with the capability to generate high-quality 3D content across various categories. In order to represent each of the $\sim 300\text{K}$ objects in our largest dataset we need very high-capacity decoder. As we found the relatively basic decoder of [63] produced poor reconstruction quality, we introduce the following key extensions (please consult the supplement for complete details):

- To support the diverse shapes and appearances in our target datasets, we find it crucial to increase the length of the embedding vectors learned by our decoder from 64 to 1024.
- We increase the number of residual blocks at each resolution in the autodecoder from 1 to 4.
- Finally, to harmonize the appearance of the reconstructed objects we introduce self-attention layers [74] in the second and third levels (resolutions 8^3 and 16^3).

3.2 Autodecoder Training

We train the decoder from image data through analysis-by-synthesis, with the primary objective of minimizing the difference between the decoder’s rendered images and the training images. We render RGB color image C using volumetric rendering [44], additionally in order to supervise silhouette of the objects we render 2D occupancy mask O .

Pyramidal Perceptual Loss. As in [62, 63], we employ a pyramidal perceptual loss based on [27] on the rendered images as our primary reconstruction loss:

$$\mathcal{L}_{\text{rec}}(\hat{C}, C) = \sum_{l=0}^L \sum_{i=0}^I \left| \text{VGG}_i(\text{D}_l(\hat{C})) - \text{VGG}_i(\text{D}_l(C)) \right|, \quad (1)$$

where $\hat{C}, C \in [0, 1]^{H \times W \times 3}$ are the RGB rendered and training images of resolution $H \times W$, respectively; VGG_i is the i^{th} -layer of a pre-trained VGG-19 [64] network; and operator D_l downsamples images to the resolution for pyramid level l .

Foreground Supervision. Since we only interested in modeling single objects, in all the datasets considered in this work, we remove the background. However if the color of the object is black (which corresponds to the absence of density), the network can make the object semi-transparent. To improve the overall shape of the reconstructed objects, we make use of a foreground supervision loss. Using binary foreground masks (estimated by an off-the-shelf matting method [40], Segment Anything [35] or synthetic ground-truth masks, depending on the dataset), we apply an L1 loss on the rendered occupancy map to match that of the mask corresponding to the image.

$$\mathcal{L}_{\text{seg}}(\hat{O}, O) = \frac{1}{HW} \|O - \hat{O}\|_1, \quad (2)$$

where $\hat{O}, O \in [0, 1]^{H \times W}$ are the inferred and ground-truth occupancy masks, respectively. We provide visual comparison of the inferred geometry for this loss in the supplement.

Multi-Frame Training. Because our new decoder have a large capacity, generating a volume incur much larger overhead compared to rendering an image based on this volume (which mostly consists of tri-linear sampling of the voxel cube). Thus, rather than rendering a single view for the canonical representation of the target object in each batch, we instead render 4 views for each object in the batch. This technique incurs no significant overhead, and effectively increases the batch size four times. As an added benefit, we find that this technique improves on the overall quality of the generated results, since it significantly reduce batch variance. We ablate this technique and our key architectural design choices, showing their effect on the sample quality (Sec. 4.3, Tab. 2).

Learning Non-Rigid Objects. For articulated, non-rigid objects, *e.g.* videos of human subjects, we must model a subject’s shape and local motion from dynamic poses, as well as the corresponding non-rigid deformation of local regions. Following [63], we assume these sequences can be decomposed into a set of N_p smaller, rigid components (10 in our experiments) whose poses can be estimated for consistent alignment in the canonical 3D space. The camera poses for each component are estimated and progressively refined during training, using a combination of learned 3D keypoints for each component of the depicted subject and the corresponding 2D projections predicted in each image. This estimation is performed via a differentiable Perspective-n-Point (PnP) algorithm [36].

To combine these components with plausible deformations, we employ a learned volumetric linear blend skinning (LBS) operation. We introduce a voxel grid $V^{LBS} \in \mathbb{R}^{S^3 \times N_p}$ to represent the skinning weights for each deformation components. As we assume no prior knowledge about the content or assignment of object components, the skinning weights for each component are also estimated during training. Please see the supplement for additional details.

3.3 Latent 3D Diffusion

Architecture. Our diffusion model architecture extends prior work on diffusion in a 2D space [32] to the latent 3D space. We implement its 2D operations, including convolutions and self-attention layers, in our 3D decoder space. In the text-conditioning experiments, after the self-attention layer, we use a cross-attention layer similar to that of [59]. Please see the supplement for more details.

Feature Processing. One of our key observation is that the features F in the latent space of the 3D autodecoder have a bell-shaped distribution (see the supplement), which eliminates the need to enforce any form of prior on it, *e.g.* as in [59]. Operating in the latent space without a prior enables training a single autodecoder for each of the possible latent diffusion resolutions. However, we observe that the feature distribution F has very long tails. We hypothesise this is because the final

density values inferred by the network do not have any natural bounds, and thus can fall within any range. In fact, the network is encouraged to make such predictions, as they have the sharpest boundaries between the surface and empty regions. However, to allow for a uniform set of diffusion hyper-parameters for all datasets and all trained autodecoders, we must normalize their features into the same range. This is equivalent to computing the center and the scale of the distribution. Note that, due to the very long-tailed feature distribution, typical mean and standard deviation statistics will be heavily biased. We thus propose a robust alternative based on the feature distribution quantiles. We take the *median* m as the center of the distribution and approximate its scale using the Normalized InterQuartile Range (IQR) [78] for a normal distribution: $0.7413 \times IQR$. Before using the features F for diffusion, we normalize them to $\hat{F} = \frac{(F-m)}{IQR}$. During inference, when producing the final volumes we de-normalize them as $\hat{F} \times IQR + m$. We call this method *robust normalization*. Please see the supplement for an evaluation of its impact.

Sampling for Object Generation. During inference we rely on the sampling method from EDM [32], with several slight modifications. We fix EDM’s hyperparameter matching the dataset’s distribution to 0.5 regardless of the experiment, and modify the feature statistics in our feature processing step. We also introduce classifier free guidance [23] for our text-conditioning experiments (Sec. 4.5). We found that setting the weight equal to 3 yields good results across all datasets.

4 Results and Evaluations

In this section, we evaluate our method on multiple diverse datasets (see Sec. 4.1) for both unconditional 4.2 and conditional settings 4.5. We also ablate the design choices in our autodecoder and diffusion in Secs. 4.3 and 4.4, respectively.

4.1 Datasets and Data Processing

Below we describe the datasets used for our evaluations. We mostly evaluate our method on datasets of synthetic renderings of 3d objects [11, 53, 12]. However, we also provide results on a challenging video dataset of dynamic human subjects [83] and dataset of static object videos [85].

ABO Tables. Following [45], we evaluate our approach on renderings of objects from the Tables subset of the Amazon Berkeley Objects (ABO) dataset [11], consisting of 1, 676 training sequences with 91 renderings per sequence, for a total of 152, 516 renderings.

PhotoShape Chairs. Also as in [45], we use images from the Chairs subset of the PhotoShape dataset [53], totaling 3, 115, 200 frames, with 200 renderings for each of 15, 576 chair models.

Objaverse. This dataset [12] contains $\sim 800K$ publicly available 3D models. As the of the object geometry and appearance varies, we use a manually-filtered subset of $\sim 300K$ unique objects (see supplement for details). We render 6 images per training object, for a total of ~ 1.8 million frames.

MVImgNet. For this dataset [85], we use ~ 6.5 million frames from 219, 188 videos of real-world objects from 239 categories, with an average of 30 frames each. We use Grounded Segment Anything [41, 35] for background removal, then apply filtering (see supplement) to remove objects with failed segmentation. This process results in 206, 990 usable objects.

CelebV-Text. The CelebV-Text dataset [83] consists of $\sim 70K$ sequences of high-quality videos of celebrities captured in in-the-wild environments, lighting, motion, and poses. They generally depict the head, neck, and upper-torso region, but contain more challenging pose and motion variation than prior datasets, *e.g.* VoxCeleb [46]. We use the robust video matting framework of [40] to obtain our masks for foreground supervision (Sec. 3.2). Some sample filtering (described in the supplement) was needed for sufficient video quality and continuity for training. This produced $\sim 44.4K$ unique videos, with an average of ~ 373 frames each, totaling $\sim 16.6M$ frames.

Camera Parameters. For training, we use the camera parameters used to render each synthetic object dataset, and the estimated parameters provided for the real video sequences in MVImgNet, adjusted to center and scale the content to our rendering volume, (see supplement for details). For the human videos in CelebV-Text, we train an additional pose estimator along with the autodecoder G to predict poses for each articulated region per frame, such that all objects can be aligned in the canonical space (Sec. 3.2). Note that for creating dynamic 3D video, we can use sequences of poses transferred from the real video of another person from the dataset.

Method	PhotoShape Chairs [53]		ABO Tables [11]		Model Variant	PSNR \uparrow	LPIPS \downarrow
	FID \downarrow	KID \downarrow	FID \downarrow	KID \downarrow			
π -GAN [5]	52.71	13.64	41.67	13.81	Ours	27.719	6.255
EG3D [6]	16.54	8.412	31.18	11.67	- Multi-Frame Training	27.176	6.855
DiffRF [45]	15.95	7.935	27.06	10.03	- Self-Attention	27.335	6.738
Ours	11.28	4.714	18.44	6.854	- Increased Depth	27.24	6.924
					- Embedding Length (1024 \rightarrow 64)	25.985	8.332

Table 1: Results on the synthetic PhotoShape Chairs [53] and ABO Tables [11] datasets. Overall, our method outperforms state-of-the-art GAN-based and diffusion-based approaches. KID scores are multiplied by 10^3 .

Table 2: Our 3D autodecoder ablation results. “-” indicates this component has been removed. As we remove each sequentially, the top row depicts results for the unmodified architecture and training procedure. LPIPS results are multiplied by 10^2 .

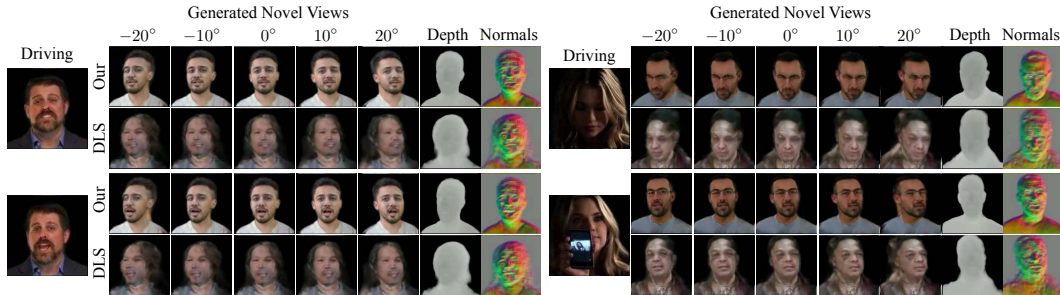


Figure 2: Qualitative comparisons with Direct Latent Sampling (DLS) [63] on CelebV [83]. We show the two driving videos for two random identities: the top identity in each block is generated by our method, the bottom identity in each block is generated by DLS [63]. We also show the rendered depth and normals.

4.2 Unconditional Image Generation

Synthetic Datasets. Following the evaluation protocol of [45], we report results on the ABO Tables and PhotoShape Chairs datasets. These results on single-category, synthetically rendered datasets that are relatively small compared to the others, demonstrate that our approach also performs well with smaller, more homogeneous data. We render 10 views of 1K samples from each dataset, and report the Fréchet Inception Distance (FID) [22] and Kernel Inception Distance (KID) [2] when compared to 10 randomly selected ground-truth images from each training sequence. We report the results compared to both GAN-based [5, 6] and more recent diffusion-based approaches [45] methods, as seen in Tab. 1. We see that our method significantly outperforms state-of-the-art methods using both metrics on the Tables dataset, and achieves better or comparable results on the Chairs dataset.

Large-Scale Datasets. We run tests on the large-scale datasets described above: MVMingNet, CelebV-Text and Objaverse. For each dataset, we render 5 images from random poses for each of 10K generated samples. We report the FID and KID for these experiments compared to 5 ground-truth images for each of 10K training objects. As no prior work demonstrates the ability to generalize to such large-scale datasets, we compare our model against directly sampling the 1D latent space of our base autodecoder architecture (using noise vectors generated from a standard normal distribution). This method of 3D generation was shown to work reasonably well [63]. We also evaluate our approach with different numbers of diffusion steps (16, 32 and 64). The results can be seen in Tab. 3. Visually, we compare with [63] in Fig. 2. Our qualitative results show substantially higher fidelity, quality of geometry and texture. We can also see that when identities are sampled directly in the 1D latent space, the normals and depth are significantly less sharp, indicating that there exist spurious density in the sampled volumes. Tab. 3 further supports this observation: both the FID and KID are significantly lower than those from direct sampling, and generally improve with additional steps.

Method	CelebV-Text [83]		MVMingNet [85]		Objaverse [12]	
	FID \downarrow	KID \downarrow	FID \downarrow	KID \downarrow	FID \downarrow	KID \downarrow
Direct Latent Sampling [63]	69.21	73.74	97.51	69.22	72.76	53.68
Ours - 16 Steps	48.01	49.49	62.21	39.94	47.49	32.44
Ours - 32 Steps	49.74	46.2	51.26	28.45	43.68	31.7
Ours - 64 Steps	50.27	47.72	43.85	23.91	40.49	29.37

Table 3: Results on large-scale multi-view image (Objaverse [12] & MVMingNet [85]) and monocular video (CelebV-Text [83]) datasets. The KID score is multiplied by 10^3 .

4.3 Autodecoder Ablation

We conduct an ablation study on the key design choices for our autodecoder architecture and training. Starting with the final version, we subtract the each component described in Sec. 3.1. We then train a model on the PhotoShape Chairs dataset and render 4 images for each of the $\sim 15.5\text{K}$ object embeddings.

Tab. 2 provides the the PSNR [26] and LPIPS [86] reconstruction metrics. We find that the final version of our process significantly outperforms the base architecture [63] and training process. While the largest improvement comes from our increase in the embedding size, we see that simply removing the multi-frame training causes a noticeable drop in quality by each metric. Interestingly, removing the self-attention layers marginally increases the PSNR and lowers the LPIPS. This is likely due to the increased complexity in training caused by these layers, which for a dataset of this size, may be unnecessary. For large-scale datasets, we observed significant improvement with this feature. Both decreasing the depth of the residual convolution blocks and reducing the embedding size cause noticeable drops in the overall quality, particularly the latter. This suggests that the additional capacity provided by these components is impactful, even on a smaller dataset.

4.4 Diffusion Ablation

We also perform ablation on our diffusion process, evaluating the effect of the choice of the number of diffusion steps (16, 32, and 64), and the autodecoder resolution at which we perform diffusion (4^3 , 8^3 , and 16^3). For these variants, we follow the generation quality training and evaluation protocol on the PhotoShape Chairs (Sec. 4.2), except that we disable stochasticity in our sampling during inference for more consistent performance across these tests. Each model was trained using roughly the same amount of time and computation. Fig. 3 shows the results. Interestingly, we can see a clear distinction between the results obtained from diffusion at the earlier or later autodecoder stages, and those from our the results with resolution 8^3 . We hypothesize that at lowest resolution layers overfit to the training dataset, thus when processing novel objects via diffusion, the quality degrades significantly. Training at a higher resolution requires substantial resources, limiting the convergence seen in a reasonable amount of time. The number of sampling steps has a smaller, more variable impact. Going from 16 to 32 steps improves the results with a reasonable increase in inference time, but at 64 steps, the largest improvement is at the 16^3 resolution, which requires more than 30 seconds per sample. Our chosen diffusion resolution of 8^3 achieves the best results, allowing for high sample quality at 64 steps (used in our other experiments) with only ~ 8 seconds of computation, but provides reasonable results with 32 steps in ~ 4 seconds.

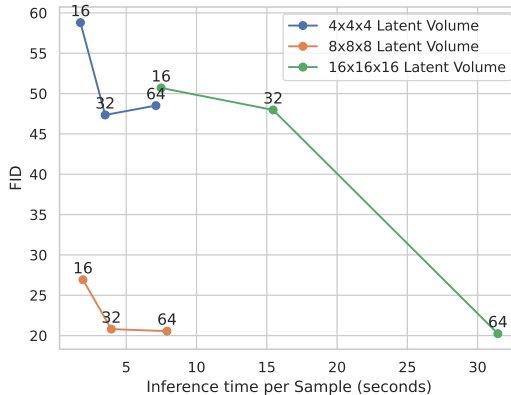


Figure 3: Impact of diffusion resolution and number of sampling steps on sample quality and inference time.

4.5 Conditional Image Generation

Finally, we train diffusion models with text-conditioning. For MVImgNet and Objaverse, we generate the text with an off-the-shelf captioning system [87]. Qualitative results for MVImgNet and Objaverse are in Figs. 4 and 5, respectively. We can see that in all cases, our method generate objects with reasonable geometry that generally follow the prompt. However, some details can be missing. We believe our model learns to ignore certain details from text prompts, as MiniGPT-4 often hallucinates details inconsistent with the object’s appearance. Better captioning systems should help alleviate this issue in the future.

5 Conclusion

Despite the inherent challenges in performing flexible 3D content generation for arbitrary content domains without 3D supervision, our work demonstrates this is possible with the right approach. By exploiting the inherent power of autodecoders to synthesize content in a domain without corresponding

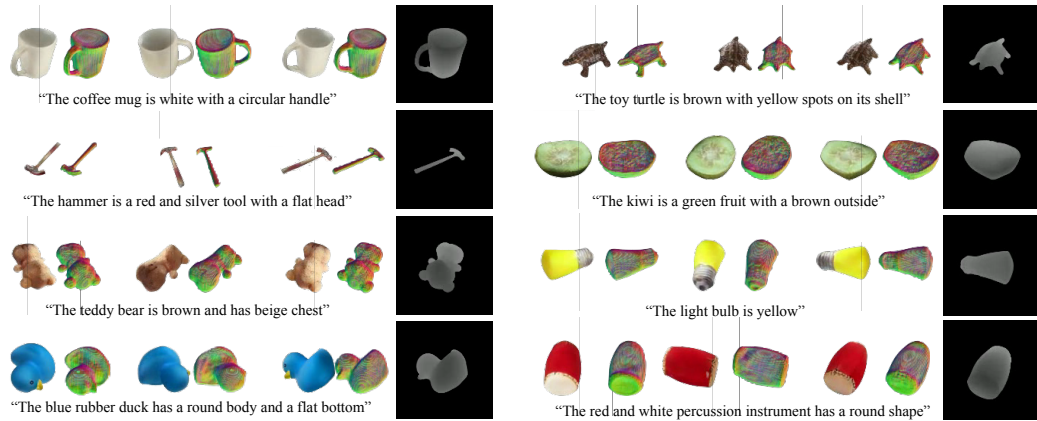


Figure 4: We show generated samples from our model trained using monocular videos from MVImgNet [85]. We show three views for each object, along with the normals for each view. We also show depth for the right-most view. Text-conditioned results are shown. Ground-truth captions are generated by MiniGPT-4 [87].

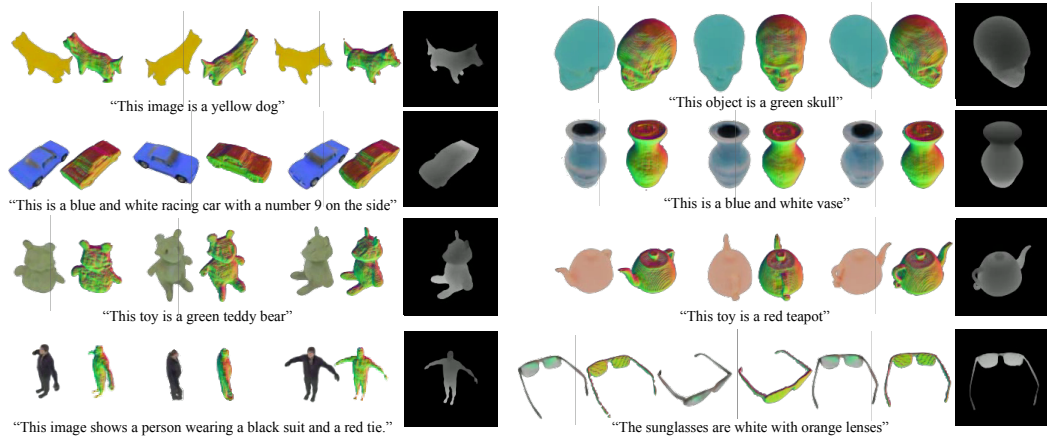


Figure 5: We show generated samples of our model trained using rendered images from Objaverse [12]. We show three views for each object, along with the normals for each view. We also show depth for the right-most view. Text-conditioned results are shown. Grouth-truth captions are generated by MiniGPT-4 [87].

encoded input, our method learns representations of the structure and appearance of diverse and complex content suitable for generating high-fidelity 3D objects using only 2D supervision. Our latent volumetric representation is conducive to 3D diffusion modeling for both conditional and unconditional generation, while enabling view-consistent rendering of the synthesized objects. As seen in our results, this generalizes well to various types of domains and datasets, from relatively small, single-category, synthetic renderings to large-scale, multi-category real-world datasets. It also supports the challenging task of generating articulated moving objects from videos. No prior work addresses each of these problems in a single framework. The progress shown here suggests there is potential to develop and extend our approach to address other open problems.

Limitations. While we demonstrate impressive and state-of-the-art results on diverse tasks and content, several challenges and limitations remain. Here we focus on images and videos with foregrounds depicting one key person or object. The generation or composition of more complex, multi-object scenes is a challenging task and an interesting direction for future work. As we require multi-view or video sequences of each object in the dataset for training, single-image datasets are not supported. Learning the appearance and geometry of diverse content for controllable 3D generation and animation from such limited data is quite challenging, especially for articulated objects. However, using general knowledge about shape, motion, and appearance extracted from datasets like ours to reduce or remove the multi-image requirement when learning to generate additional object categories may be feasible with further exploration. This would allow the generation of content learned from image datasets of potentially unbounded size and diversity.

Broader Impact. Our work shares similar concerns with other generative modeling efforts, *e.g.*, potential exploitation for misleading content. As with all such learning-based methods, biases in training datasets may be reflected in the generated content. Appropriate caution must be applied when using this method to avoid this when it may be harmful, *e.g.* human generation. Care must be taken to only use this method on public data, as the privacy of training subjects may be compromised if our framework is used to recover their identities. The environmental impact of methods requiring substantial energy for training and inference is also a concern. However, our approach makes our tasks more tractable by removing the need for the curation and processing of large-scale 3D datasets, and is thus more amenable to efficient use than methods requiring such input.

Acknowledgements We would like to thank Michael Vasilkovsky for preparing the Objaverse renderings, and Colin Eles for his support with infrastructure. Moreover, we would like to thank Norman Müller, author of DiffRF paper, for his invaluable help with setting up the DiffRF baseline, the ABO Tables and PhotoShape Chairs datasets, and the evaluation pipeline as well as answering all related questions. A true marvel of a scientist. Finally, Evan would like to thank Claire and Gio for making the best cappuccinos and fueling up this research.

References

- [1] Panos Achlioptas, Olga Diamanti, Ioannis Mitliagkas, and Leonidas Guibas. Learning Representations and Generative Models for 3D Point Clouds. In *Proceedings of the International Conference on Machine Learning*, 2018.
- [2] Mikołaj Bińkowski, Dougal J. Sutherland, Michael Arbel, and Arthur Gretton. Demystifying MMD GANs. In *Proceedings of the IEEE Conference on Computer Vision and Pattern Recognition*, 2018.
- [3] Piotr Bojanowski, Armand Joulin, David Lopez-Paz, and Arthur Szlam. Optimizing the latent space of generative networks. In *arXiv*, 2017.
- [4] Andrew Brock, Jeff Donahue, and Karen Simonyan. Large scale gan training for high fidelity natural image synthesis. In *arXiv*, 2018.
- [5] Eric R Chan, Marco Monteiro, Petr Kellnhofer, Jiajun Wu, and Gordon Wetzstein. pi-GAN: Periodic Implicit Generative Adversarial Networks for 3D-Aware Image Synthesis. In *Proceedings of the IEEE Conference on Computer Vision and Pattern Recognition*, 2021.
- [6] Eric R. Chan, Connor Z. Lin, Matthew A. Chan, Koki Nagano, Boxiao Pan, Shalini De Mello, Orazio Gallo, Leonidas Guibas, Jonathan Tremblay, Sameh Khamis, Tero Karras, and Gordon Wetzstein. Efficient Geometry-aware 3D Generative Adversarial Networks. In *Proceedings of the IEEE Conference on Computer Vision and Pattern Recognition*, 2022.
- [7] Angel X. Chang, Thomas Funkhouser, Leonidas Guibas, Pat Hanrahan, Qixing Huang, Zimo Li, Silvio Savarese, Manolis Savva, Shuran Song, Hao Su, Jianxiong Xiao, Li Yi, and Fisher Yu. ShapeNet: An Information-Rich 3D Model Repository. In *arXiv*, 2015.
- [8] Nanxin Chen, Yu Zhang, Heiga Zen, Ron J Weiss, Mohammad Norouzi, and William Chan. WaveGrad: Estimating Gradients for Waveform Generation. In *Proceedings of the IEEE Conference on Computer Vision and Pattern Recognition*, 2021.
- [9] Rui Chen, Yongwei Chen, Ningxin Jiao, and Kui Jia. Fantasia3D: Disentangling Geometry and Appearance for High-quality Text-to-3D Content Creation. In *arXiv*, 2023.
- [10] Yen-Chi Cheng, Hsin-Ying Lee, Sergey Tuyakov, Alex Schwing, and Liangyan Gui. SDFusion: Multimodal 3d shape completion, reconstruction, and generation. In *Proceedings of the IEEE Conference on Computer Vision and Pattern Recognition*, 2023.
- [11] Jasmine Collins, Shubham Goel, Kenan Deng, Achleshwar Luthra, Leon Xu, Erhan Gundogdu, Xi Zhang, Tomas F Yago Vicente, Thomas Dideriksen, Himanshu Arora, Matthieu Guillaumin, and Jitendra Malik. ABO: Dataset and Benchmarks for Real-World 3D Object Understanding. In *Proceedings of the IEEE Conference on Computer Vision and Pattern Recognition*, 2022.
- [12] Matt Deitke, Dustin Schwenk, Jordi Salvador, Luca Weihs, Oscar Michel, Eli VanderBilt, Ludwig Schmidt, Kiana Ehsani, Aniruddha Kembhavi, and Ali Farhadi. Objaverse: A Universe of Annotated 3D Objects. In *arXiv*, 2022.

- [13] Jia Deng, Wei Dong, Richard Socher, Li-Jia Li, Kai Li, and Li Fei-Fei. Imagenet: A large-scale hierarchical image database. In *Proceedings of the IEEE Conference on Computer Vision and Pattern Recognition*, 2009.
- [14] Sridhar Devadas and Konstantinos Daskalakis. MIT 6.006, Lecture 5: Hashing I: Chaining, Hash Functions, 2009.
- [15] Prafulla Dhariwal and Alexander Nichol. Diffusion Models Beat Gans on Image Synthesis. In *Proceedings of the Neural Information Processing Systems Conference*, 2021.
- [16] Tim Dockhorn, Arash Vahdat, and Karsten Kreis. Score-based generative modeling with critically-damped langevin diffusion. In *Proceedings of the IEEE Conference on Computer Vision and Pattern Recognition*, 2022.
- [17] William Falcon et al. PyTorch Lightning. *GitHub*. Note: <https://github.com/PyTorchLightning/pytorch-lightning>, 3, 2019.
- [18] Seth* Forsgren and Hayk* Martiros. Riffusion - Stable diffusion for real-time music generation, 2022. URL <https://riffusion.com/about>.
- [19] Ian Goodfellow, Jean Pouget-Abadie, Mehdi Mirza, Bing Xu, David Warde-Farley, Sherjil Ozair, Aaron Courville, and Yoshua Bengio. Generative adversarial nets. In *Proceedings of the Neural Information Processing Systems Conference*, 2014.
- [20] William Harvey, Saeid Naderiparizi, Vaden Masrani, Christian Dietrich Weillbach, and Frank Wood. Flexible Diffusion Modeling of Long Videos. In *Proceedings of the Neural Information Processing Systems Conference*, 2022.
- [21] Yingqing He, Tianyu Yang, Yong Zhang, Ying Shan, and Qifeng Chen. Latent video diffusion models for high-fidelity long video generation. In *arXiv*, 2023.
- [22] Martin Heusel, Hubert Ramsauer, Thomas Unterthiner, Bernhard Nessler, and Sepp Hochreiter. GANs Trained by a Two Time-Scale Update Rule Converge to a Local Nash Equilibrium. In *Proceedings of the Neural Information Processing Systems Conference*, 2017.
- [23] Jonathan Ho and Tim Salimans. Classifier-free diffusion guidance. In *arXiv*, 2022.
- [24] Jonathan Ho, Ajay Jain, and Pieter Abbeel. Denoising diffusion probabilistic models. In *Proceedings of the Neural Information Processing Systems Conference*, 2020.
- [25] Jonathan Ho, Tim Salimans, Alexey A. Gritsenko, William Chan, Mohammad Norouzi, and David J. Fleet. Video Diffusion Models. In *Proceedings of the IEEE Conference on Computer Vision and Pattern Recognition*, 2022.
- [26] A. Horé and D. Ziou. Image quality metrics: Psnr vs. ssim. In *Proceedings of the International Conference on Pattern Recognition*, 2010.
- [27] Justin Johnson, Alexandre Alahi, and Li Fei-Fei. Perceptual Losses for Real-Time Style Transfer and Super-Resolution. In *Proceedings of the European Conference on Computer Vision*, 2016.
- [28] Tero Karras, Timo Aila, Samuli Laine, and Jaakko Lehtinen. Progressive growing of GANs for improved quality, stability, and variation. In *Proceedings of the IEEE Conference on Computer Vision and Pattern Recognition*, 2018.
- [29] Tero Karras, Samuli Laine, and Timo Aila. A style-based generator architecture for generative adversarial networks. In *Proceedings of the IEEE Conference on Computer Vision and Pattern Recognition*, 2019.
- [30] Tero Karras, Miika Aittala, Janne Hellsten, Samuli Laine, Jaakko Lehtinen, and Timo Aila. Training generative adversarial networks with limited data. In *arXiv*, 2020.
- [31] Tero Karras, Samuli Laine, Miika Aittala, Janne Hellsten, Jaakko Lehtinen, and Timo Aila. Analyzing and Improving the Image Quality of StyleGAN. In *Proceedings of the IEEE Conference on Computer Vision and Pattern Recognition*, 2020.
- [32] Tero Karras, Miika Aittala, Timo Aila, and Samuli Laine. Elucidating the Design Space of Diffusion-Based Generative Models. In *Proceedings of the Neural Information Processing Systems Conference*, 2022.
- [33] Diederik P. Kingma and Jimmy Ba. Adam: A Method for Stochastic Optimization. In *Proceedings of the IEEE Conference on Computer Vision and Pattern Recognition*, 2015.

- [34] Diederik P Kingma and Max Welling. Auto-encoding variational bayes. In *Proceedings of the IEEE Conference on Computer Vision and Pattern Recognition*, 2014.
- [35] Alexander Kirillov, Eric Mintun, Nikhila Ravi, Hanzi Mao, Chloe Rolland, Laura Gustafson, Tete Xiao, Spencer Whitehead, Alexander C. Berg, Wan-Yen Lo, Piotr Dollár, and Ross Girshick. Segment Anything. In *arXiv*, 2023.
- [36] Vincent Lepetit, Francesc Moreno-Noguer, and Pascal Fua. EPnP: An Accurate O(n) Solution to the PnP Problem. In *International Journal of Computer Vision*, 2009.
- [37] J. P. Lewis, Matt Corder, and Nickson Fong. Pose Space Deformation: A Unified Approach to Shape Interpolation and Skeleton-Driven Deformation. In *ACM Transactions on Graphics*, 2000.
- [38] Chen-Hsuan Lin, Wei-Chiu Ma, Antonio Torralba, and Simon Lucey. BARF: Bundle-Adjusting Neural Radiance Fields. In *Proceedings of the IEEE International Conference on Computer Vision*, 2021.
- [39] Chen-Hsuan Lin, Jun Gao, Luming Tang, Towaki Takikawa, Xiaohui Zeng, Xun Huang, Karsten Kreis, Sanja Fidler, Ming-Yu Liu, and Tsung-Yi Lin. Magic3D: High-Resolution Text-to-3D Content Creation. In *Proceedings of the IEEE Conference on Computer Vision and Pattern Recognition*, 2023.
- [40] S. Lin, L. Yang, I. Saleemi, and S. Sengupta. Robust High-Resolution Video Matting with Temporal Guidance. In *Proceedings of the Winter Conference on Applications of Computer Vision*, 2022.
- [41] Shilong Liu, Zhaoyang Zeng, Tianhe Ren, Feng Li, Hao Zhang, Jie Yang, Chunyuan Li, Jianwei Yang, Hang Su, Jun Zhu, et al. Grounding DINO: Marrying DINO with Grounded Pre-Training for Open-Set Object Detection. In *arXiv*, 2023.
- [42] William E. Lorensen and Harvey E. Cline. Marching Cubes: A High Resolution 3D Surface Construction Algorithm. In *ACM Transactions on Graphics*, 1987.
- [43] Kangfu Mei and Vishal M. Patel. VIDM: Video Implicit Diffusion Models. In *Association for the Advancement of Artificial Intelligence Conference*, 2023.
- [44] Ben Mildenhall, Pratul P Srinivasan, Matthew Tancik, Jonathan T Barron, Ravi Ramamoorthi, and Ren Ng. NeRF: Representing scenes as Neural Radiance Fields for View Synthesis. In *Proceedings of the European Conference on Computer Vision*, 2020.
- [45] Norman Müller, Yawar Siddiqui, Lorenzo Porzi, Samuel Rota Bulò, Peter Kotschieder, and Matthias Nießner. DiffRF: Rendering-Guided 3D Radiance Field Diffusion. In *Proceedings of the IEEE Conference on Computer Vision and Pattern Recognition*, 2023.
- [46] Arsha Nagrani, Joon Son Chung, Weidi Xie, and Andrew Senior. VoxCeleb: Large-scale speaker verification in the wild. *Computer Science and Language*, 2019.
- [47] Thu Nguyen-Phuoc, Chuan Li, Lucas Theis, Christian Richardt, and Yong-Liang Yang. HoloGAN: Unsupervised Learning of 3D Representations From Natural Images. In *Proceedings of the IEEE International Conference on Computer Vision*, 2019.
- [48] Thu Nguyen-Phuoc, Christian Richardt, Long Mai, Yong-Liang Yang, and Niloy Mitra. Blockgan: Learning 3d object-aware scene representations from unlabelled images. In *arXiv*, 2020.
- [49] Alexander Quinn Nichol and Prafulla Dhariwal. Improved denoising diffusion probabilistic models. In *ICML*, 2021.
- [50] Michael Niemeyer and Andreas Geiger. GIRAFFE: Representing Scenes as Compositional Generative Neural Feature Fields. In *Proceedings of the IEEE Conference on Computer Vision and Pattern Recognition*, 2021.
- [51] Evangelos Ntavelis, Mohamad Shahbazi, Iason Kastanis, Radu Timofte, Martin Danelljan, and Luc Van Gool. StyleGenes: Discrete and Efficient Latent Distributions for GANs. In *arXiv*, 2023.
- [52] Anton Obukhov, Maximilian Seitzer, Po-Wei Wu, Semen Zhydenko, Jonathan Kyl, and Elvis Yu-Jing Lin. High-fidelity performance metrics for generative models in PyTorch, 2020. URL <https://github.com/toshas/torch-fidelity>. Version: 0.3.0, DOI: 10.5281/zenodo.4957738.
- [53] Keunhong Park, Konstantinos Rematas, Ali Farhadi, and Steven M. Seitz. PhotoShape: Photorealistic Materials for Large-Scale Shape Collections. In *ACM Transactions on Graphics*, 2018.
- [54] Adam Paszke, Sam Gross, Soumith Chintala, Gregory Chanan, Edward Yang, Zachary DeVito, Zeming Lin, Alban Desmaison, Luca Antiga, and Adam Lerer. Automatic Differentiation in PyTorch, 2017.

- [55] Adam Paszke, Sam Gross, Francisco Massa, Adam Lerer, James Bradbury, Gregory Chanan, Trevor Killeen, Zeming Lin, Natalia Gimelshein, Luca Antiga, Alban Desmaison, Andreas Kopf, Edward Yang, Zachary DeVito, Martin Raison, Alykhan Tejani, Sasank Chilamkurthy, Benoit Steiner, Lu Fang, Junjie Bai, and Soumith Chintala. PyTorch: An Imperative Style, High-Performance Deep Learning Library. In *Proceedings of the Neural Information Processing Systems Conference*, 2019.
- [56] Poole, Ben and Jain, Ajay and Barron, Jonathan T. and Mildenhall, Ben. Dreamfusion: Text-to-3d using 2d diffusion. In *arXiv*, 2022.
- [57] Colin Raffel, Noam Shazeer, Adam Roberts, Katherine Lee, Sharan Narang, Michael Matena, Yanqi Zhou, Wei Li, and Peter J. Liu. Exploring the Limits of Transfer Learning with a Unified Text-to-Text Transformer. In *The Journal of Machine Learning Research*, 2020.
- [58] Nikhila Ravi, Jeremy Reizenstein, David Novotny, Taylor Gordon, Wan-Yen Lo, Justin Johnson, and Georgia Gkioxari. Accelerating 3D Deep Learning with PyTorch3D. In *arXiv*, 2020.
- [59] Robin Rombach, Andreas Blattmann, Dominik Lorenz, Patrick Esser, and Björn Ommer. High-Resolution Image Synthesis With Latent Diffusion Models. In *Proceedings of the IEEE Conference on Computer Vision and Pattern Recognition*, 2022.
- [60] Johannes Lutz Schönberger and Jan-Michael Frahm. Structure-from-Motion Revisited. In *Proceedings of the IEEE Conference on Computer Vision and Pattern Recognition*, 2016.
- [61] Katja Schwarz, Yiyi Liao, Michael Niemeyer, and Andreas Geiger. GRAF: Generative Radiance Fields for 3D-Aware Image Synthesis. In *Proceedings of the Neural Information Processing Systems Conference*, 2020.
- [62] Aliaksandr Siarohin, Stéphane Lathuilière, Sergey Tulyakov, Elisa Ricci, and Nicu Sebe. First Order Motion Model for Image Animation. In *Proceedings of the Neural Information Processing Systems Conference*, 2019.
- [63] Aliaksandr Siarohin, Willi Menapace, Ivan Skorokhodov, Kyle Olszewski, Hsin-Ying Lee, Jian Ren, Menglei Chai, and Sergey Tulyakov. Unsupervised Volumetric Animation. In *Proceedings of the IEEE Conference on Computer Vision and Pattern Recognition*, 2023.
- [64] Karen Simonyan and Andrew Zisserman. Very deep convolutional networks for large-scale image recognition. In *arXiv*, 2014.
- [65] Ivan Skorokhodov, Sergey Tulyakov, and Mohamed Elhoseiny. Stylegan-v: A continuous video generator with the price, image quality and perks of stylegan2. In *Proceedings of the IEEE Conference on Computer Vision and Pattern Recognition*, 2022.
- [66] Ivan Skorokhodov, Sergey Tulyakov, Yiqun Wang, and Peter Wonka. EpiGRAF: Rethinking Training of 3D GANs. In *Proceedings of the Neural Information Processing Systems Conference*, 2022.
- [67] Ivan Skorokhodov, Aliaksandr Siarohin, Yinghao Xu, Jian Ren, Hsin-Ying Lee, Peter Wonka, and Sergey Tulyakov. 3D Generation on ImageNet. In *Proceedings of the IEEE Conference on Computer Vision and Pattern Recognition*, 2023.
- [68] Jascha Sohl-Dickstein, Eric Weiss, Niru Maheswaranathan, and Surya Ganguli. Deep unsupervised learning using nonequilibrium thermodynamics. In *ICML*, 2015.
- [69] Jiaming Song, Chenlin Meng, and Stefano Ermon. Denoising Diffusion Implicit Models. In *Proceedings of the IEEE Conference on Computer Vision and Pattern Recognition*, 2021.
- [70] Yang Song and Stefano Ermon. Generative modeling by estimating gradients of the data distribution. In *Proceedings of the Neural Information Processing Systems Conference*, 2019.
- [71] Yang Song, Jascha Sohl-Dickstein, Diederik P Kingma, Abhishek Kumar, Stefano Ermon, and Ben Poole. Score-based generative modeling through stochastic differential equations. In *Proceedings of the IEEE Conference on Computer Vision and Pattern Recognition*, 2021.
- [72] Yu Tian, Jian Ren, Menglei Chai, Kyle Olszewski, Xi Peng, Dimitris N. Metaxas, and Sergey Tulyakov. A good image generator is what you need for high-resolution video synthesis. In *Proceedings of the IEEE Conference on Computer Vision and Pattern Recognition*, 2021.
- [73] Arash Vahdat, Karsten Kreis, and Jan Kautz. Score-based generative modeling in latent space. In *Proceedings of the Neural Information Processing Systems Conference*, 2021.

- [74] Vaswani, Ashish and Shazeer, Noam and Parmar, Niki and Uszkoreit, Jakob and Jones, Llion and Gomez, Aidan N and Kaiser, Łukasz and Polosukhin, Illia. Attention is all you need. In *Proceedings of the Neural Information Processing Systems Conference*, 2017.
- [75] Vikram Voleti, Alexia Jolicoeur-Martineau, and Christopher Pal. MCVD: Masked Conditional Video Diffusion for Prediction, Generation, and Interpolation. In *Proceedings of the Neural Information Processing Systems Conference*, 2022.
- [76] Zirui Wang, Shangzhe Wu, Weidi Xie, Min Chen, and Victor Adrian Prisacariu. NeRF---: Neural Radiance Fields Without Known Camera Parameters. In *arXiv*, 2021.
- [77] Chung-Yi Weng, Brian Curless, Pratul P Srinivasan, Jonathan T Barron, and Ira Kemelmacher-Shlizerman. HumanNeRF: Free-Viewpoint Rendering of Moving People from Monocular Video. In *Proceedings of the IEEE Conference on Computer Vision and Pattern Recognition*, 2022.
- [78] Dewey Lonzo Whaley III. *The Interquartile Range: Theory and Estimation*. PhD thesis, East Tennessee State University, 2005.
- [79] Zhisheng Xiao, Karsten Kreis, and Arash Vahdat. Tackling the generative learning trilemma with denoising diffusion GANs. In *Proceedings of the IEEE Conference on Computer Vision and Pattern Recognition*, 2022.
- [80] Lumin Xu, Sheng Jin, Wang Zeng, Wentao Liu, Chen Qian, Wanli Ouyang, Ping Luo, and Xiaogang Wang. Pose for Everything: Towards Category-Agnostic Pose Estimation. In *Proceedings of the European Conference on Computer Vision*, 2022.
- [81] Yang Xue, Yuheng Li, Krishna Kumar Singh, and Yong Jae Lee. GIRAFFE HD: A High-Resolution 3D-aware Generative Model. In *Proceedings of the IEEE Conference on Computer Vision and Pattern Recognition*, 2022.
- [82] Shengming Yin, Chenfei Wu, Huan Yang, Jianfeng Wang, Xiaodong Wang, Minheng Ni, Zhengyuan Yang, Linjie Li, Shuguang Liu, Fan Yang, Jianlong Fu, Gong Ming, Lijuan Wang, Zicheng Liu, Houqiang Li, and Nan Duan. NUWA-XL: Diffusion over Diffusion for eXtremely Long Video Generation. In *arXiv*, 2023.
- [83] Jianhui Yu, Hao Zhu, Liming Jiang, Chen Change Loy, Weidong Cai, and Wayne Wu. CelebV-Text: A Large-Scale Facial Text-Video Dataset. In *Proceedings of the IEEE Conference on Computer Vision and Pattern Recognition*, 2023.
- [84] Sihyun Yu, Jihoon Tack, Sangwoo Mo, Hyunsu Kim, Junho Kim, Jung-Woo Ha, and Jinwoo Shin. Generating videos with dynamics-aware implicit generative adversarial networks. In *Proceedings of the IEEE Conference on Computer Vision and Pattern Recognition*, 2022.
- [85] Xianggang Yu, Mutian Xu, Yidan Zhang, Haolin Liu, Chongjie Ye, Yushuang Wu, Zizheng Yan, Chenming Zhu, Zhangyang Xiong, Tianyou Liang, Guanying Chen, Shuguang Cui, and Xiaoguang Han. MVImgNet: A Large-scale Dataset of Multi-view Images. In *arXiv*, 2023.
- [86] Richard Zhang, Phillip Isola, Alexei A. Efros, Eli Shechtman, and Oliver Wang. The Unreasonable Effectiveness of Deep Features as a Perceptual Metric. In *Proceedings of the IEEE Conference on Computer Vision and Pattern Recognition*, 2018.
- [87] Deyao Zhu, Jun Chen, Xiaoqian Shen, Xiang Li, and Mohamed Elhoseiny. MiniGPT-4: Enhancing Vision-Language Understanding with Advanced Large Language Models. In *arXiv*, 2023.
- [88] Ye Zhu, Yu Wu, Kyle Olszewski, Jian Ren, Sergey Tulyakov, and Yan Yan. Discrete contrastive diffusion for cross-modal music and image generation. In *Proceedings of the IEEE Conference on Computer Vision and Pattern Recognition*, 2023.

A Additional Experiments and Results

A.1 Geometry Generation Evaluation

Following the point cloud evaluation protocol of [1], we measure the Coverage Score (COV) and the Minimum Matching Distance (MMD) for points sampled from our generated density volumes. Given a distance metric for two point clouds X and Y , *e.g.* the Chamfer Distance (CD),

$$\text{CD}(X, Y) = \sum_{x \in X} \min_{y \in Y} \|x - y\|_2^2 + \sum_{y \in Y} \min_{x \in X} \|x - y\|_2^2, \quad (3)$$

COV measures the *diversity* of the generated point cloud set S_g , with respect to a reference point cloud set S_r , by finding the closest neighbor in the reference set to each one in the sample set, and computing the fraction of the reference set covered by these samples:

$$\text{COV}(S_g, S_r) = \frac{|\{\arg \min_{Y \in S_r} \text{CD}(X, Y) | X \in S_g\}|}{|S_r|}. \quad (4)$$

MMD, in contrast, measures the overall *quality* of these samples, by measuring the average distance between each sampled point cloud and its closest neighbor in the reference set:

$$\text{MMD}(S_g, S_r) = \frac{1}{|S_r|} \sum_{Y \in S_r} \min_{X \in S_g} \text{CD}(X, Y). \quad (5)$$

We compute these metrics for the PhotoShape Chairs and ABO Tables datasets, comparing our generated results to points sampled from the the same reference meshes used in the data splits from the evaluations in DiffRF [45]. For each generated object, we sample 2048 points from a mesh extracted from the decoded density volume V^{Density} (see Sec. 3.1) using the Marching Cubes [42] algorithm. We use a volume of resolution 64^3 and 128^3 for training the Chairs and Tables models, respectively. However, we note that downsampling these density volumes to 32^3 , as is used in DiffRF, before applying this point-sampling operation did not noticeably impact the results of these evaluations.

The results can be seen in Tab. 4, alongside the perceptual metrics from the main paper. Interestingly, these results show that, despite the increased flexibility of our approach, and DiffRF’s restrictive use of both 2D rendering and 3D supervision on synthetic data when training their diffusion model, we obtain comparable or superior geometry compared to their approach, while substantially increasing the overall perceptual quality for these datasets. We also substantially outperform prior state-of-the-art approaches using GAN-based [5, 6] methods across both perceptual and geometric comparisons with these metrics.

Figs. 7 and 8 show qualitative comparisons between the unconditional generation results rendered using our method and DiffRF for each of these datasets. In each case, it is clear that for similar objects, our method produces more coherent and complete shapes without missing features, *e.g.* legs, and textures that are more realistic and detailed, leading to better and more consistent image synthesis results.

A.2 Foreground Supervision

For some datasets with foregrounds with complex and varying appearance which can easily be mixed with the background environment, we found it necessary to supplement our primary autodecoder reconstruction loss (Sec. 3.2) with an additional foreground supervision loss. This loss measures how well depicted objects are separated from the background during rendering. To evaluate the effect of this foreground supervision, we ran experiments on the CelebV-Text [83] dataset both with and without this loss. We conduct our training until the autodecoder has seen a total of 9 million frames from the training set, then reconstruct examples from the learned embeddings.

The result can be seen in Fig. 6. As depicted, the reconstructions without foreground supervision not only lack fidelity to the target appearance, but the estimated opacity and surfaces normals clearly show that the overall geometry is insufficiently recovered.

Method	PhotoShape Chairs [53]				ABO Tables [11]			
	FID ↓	KID ↓	COV ↑	MMD ↓	FID ↓	KID ↓	COV ↑	MMD ↓
π -GAN [5]	52.71	13.64	39.92	7.387	41.67	13.81	44.23	10.92
EG3D [6]	16.54	8.412	47.55	5.619	31.18	11.67	48.15	9.327
DiffRF [45]	15.95	7.935	58.93	4.416	27.06	10.03	61.54	7.610
Ours	11.28	4.714	64.20	4.445	18.44	6.854	60.25	6.684

Table 4: **Quantitative comparison** of unconditional generation on the PhotoShape Chairs [53] and ABO Tables [11] datasets. Our method achieves a better perceptual quality, while maintaining similar geometric quality to the state-of-the-art diffusion-based approaches. MMD and KID scores are multiplied by 10^3 .

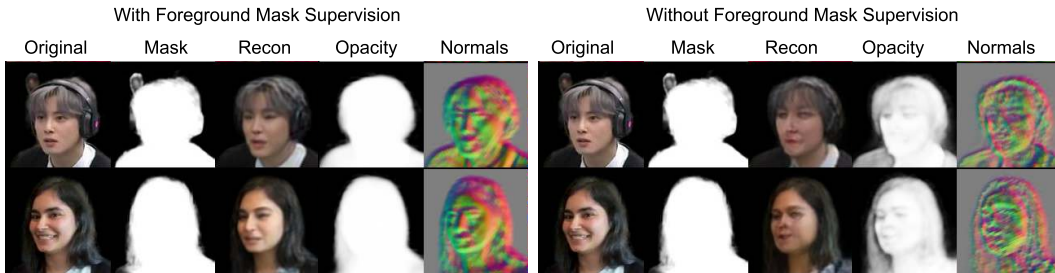


Figure 6: In real video datasets, *e.g.* CelebV-Text[83], we have a diverse set of foreground shapes and textures with a common background color. In these cases, we find that supervising the autodecoder with a foreground mask loss is important for the network to properly learn the shape of the object. Both examples shown after training for ~ 9 million frames.

A.3 Animated Results

Please see the corresponding supplementary web page for additional video results, showing consistent novel-view synthesis for rigid objects from multi-category datasets and animated articulated objects sampled using our approach, and results demonstrating both conditional and unconditional generation.

B Method Details

B.1 Volumetric Autodecoder

Volumetric Rendering. We use learnable volumetric rendering [44] to generate the final images from the final decoded volume. Given a camera intrinsic and extrinsic parameters for a target image, and the radiance field volumes generated by the decoder, for each pixel in the image, we cast a ray through the volume, sampling the color and density values to compute the color $C(\mathbf{r})$ by integrating the radiance along the ray $\mathbf{r}(t) = \mathbf{o} + t\mathbf{d}$, with near and far bounds t_n and t_f :

$$C(\mathbf{r}) = \int_{t_n}^{t_f} T(t)\delta(\mathbf{r}(t))\mathbf{c}(\mathbf{r}(t), \mathbf{d})dt, \quad (6)$$

where δ , \mathbf{c} are the density and RGB values from the radiance field volumes sampled along these rays, and $T(t) = \exp\left\{-\int_{t_n}^t \sigma(\mathbf{r}(s))ds\right\}$ is the accumulated transmittance between t_n and t .

To supervise the silhouette of objects, we also render the 2D occupancy map O using the volumetric equation:

$$O(\mathbf{r}) = \int_{t_n}^{t_f} T(t)\delta(\mathbf{r}(t))dt. \quad (7)$$

We sample 128 points across these rays for radiance field rendering during training and inference.



Figure 7: **Qualitative comparison of unconditional generation** using DiffRF [45] (left) and our approach (right) on the ABO Tables dataset [11]. In contrast to DiffRF, we train diffusion in the latent features of an autoencoder. Decoupling the expensive and demanding training from the output voxel-grid size lets us increase the resolution of our 3D representation. For this dataset, our output voxel resolution is 128^3 , compared to the 32^3 resolution of DiffRF. Our method improves the perceptual quality of the results, as it is shown in the reported FID and KID.

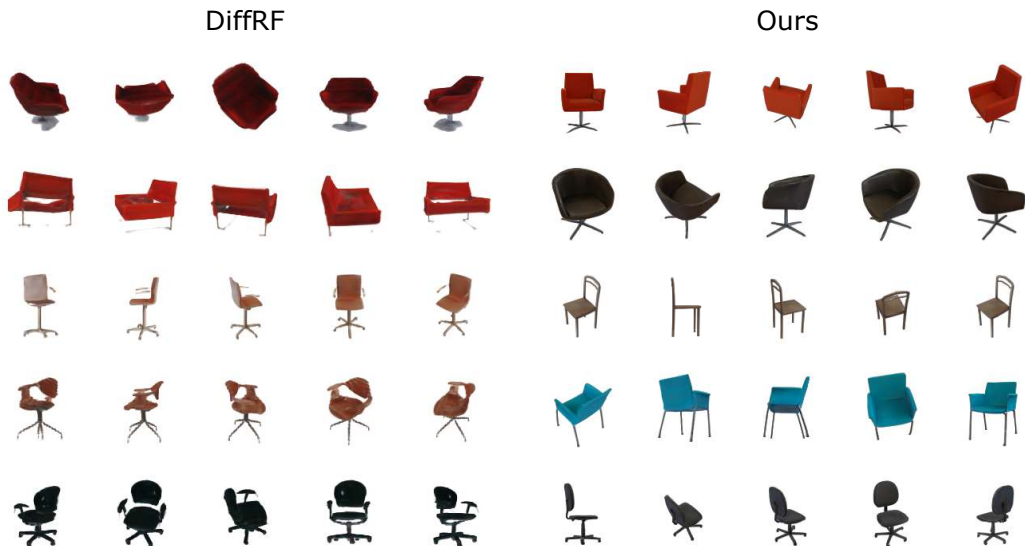


Figure 8: **Qualitative comparison of unconditional generation** using DiffRF [45] (left) and our approach (right) on the PhotoShapes Chairs dataset [53]. For this dataset, our output voxel resolution is 64^3 . As above, our results are both qualitatively and quantitatively superior.

Articulated Animation. As our approach is flexibly designed to support both rigid and articulated subjects, we employ different approaches to pose supervision to better handle each of these cases.

For articulated subjects, poses are estimated during training, using a set of learnable 3D keypoints K^{3D} and their predicted 2D projections K^{2D} in each image in an extended version of the Perspective-n-Point (PnP) algorithm [36]. To handle articulated animation, however, rather than learn a single pose per image using these points, we assume that the target subjects can be decomposed into N_p regions, each containing N_k points K_p^{3D} and their corresponding K_p^{2D} projections per image. These points are shared across all subjects, and are aligned in the learned canonical space, allowing for realistic generation and motion transfer between these subjects. This allows for learning N_p poses per-frame defining the pose of each region p relative to its pose in the learned canonical pose.

To successfully reconstruct the training images for each subject thus requires learning the appropriate canonical locations for each region’s 3D keypoints, to predict the 2D projections of these keypoints in each frame, and the pose best matching the 3D points and 2D projections for these regions. We can then use this information in our volumetric rendering framework to sample appropriately from the canonical space such that the subject’s appearance and pose are consistent and appropriate throughout their video sequence. Using this approach, this information can be learned along with our autodecoder parameters for articulated objects using the reconstruction and foreground supervision losses used for our rigid object datasets.

As noted in Sec. 3.2, to better handle non-rigid shape deformations corresponding to this articulated motion, we employ volumetric linear blend skinning (LBS) [37]. This allows us to learn the weight each component p in the canonical space contributes to a sampled point in the deformed space based on the spatial correspondence between these two spaces:

$$x_d = \sum_{p=1}^{N_p} w_p^c(x_c) (R_p x_c + \text{tr}_p), \quad (8)$$

where $T_p = [R_p, \text{tr}_p] = [R^{-1}, -R^{-1} \text{tr}]$ is the estimated pose of part p relative to the camera (where $T = [R, \text{tr}] \in \mathbb{R}^{3 \times 4}$ is the estimated camera pose with respect to our canonical volume) ; x_d is the 3D point deformed to correspond to the current pose; x_c is its corresponding point when aligned in the canonical volume; and $w_p^c(x_c)$ is the learned LBS weight for component p , sampled at position x_c in the volume, used to define this correspondence.³

Thus, for our non-rigid subjects, in addition to the density and color volumes needed to integrate Eqns. 6 and 7 above, our autodecoder learns to produce a volume $V^{LBS} \in \mathbb{R}^{S^3 \times N_p}$ containing the LBS weights for each of the N_p locally rigid regions constituting the subject.

We assign $N_k = 125$ 3D keypoints to each of the $N_p = 10$ regions. For these tests, we assume fixed camera intrinsics with a field-of-view of 0.175 radians, as in [50]. We use the differentiable Perspective-n-Point (PnP) algorithm [36] implementation from PyTorch3D [58] to accelerate this training process.

As this approach suffices for objects with standard canonical shapes (*e.g.*, human faces) performing non-rigid motion in continuous video sequences, we employ this approach for our tests on the CelebV-Text dataset. While in theory, such an approach could be used for pose estimation for rigid objects (with only 1 component) in each view, for we find that this approach is less reliable for our rigid object datasets, which contain sparse, multi-view images from randomly sampled, non-continuous camera poses, depicting content with drastically varying shapes and appearances (*e.g.*, the multi-category object datasets described below). Thus, for these objects, we use as input either known ground-truth or estimated camera poses (using [60]), for synthetic renderings or real images, respectively. While some works [76, 38, 80] perform category-agnostic object or camera pose estimation without predefined keypoints from sparse images of arbitrary objects or scenes, employing such techniques for such data is beyond the scope of this work.

Architecture. Our volumetric autodecoder architecture follows that of [63], with the key extensions described in this work. Given an embedding vector e of size 1024, we use a fully-connected layer

³In practice, as in [63], we compute an approximate solution using the inverse LBS weights following HumanNeRF [77] to avoid the excessive computation required by the direct solution.

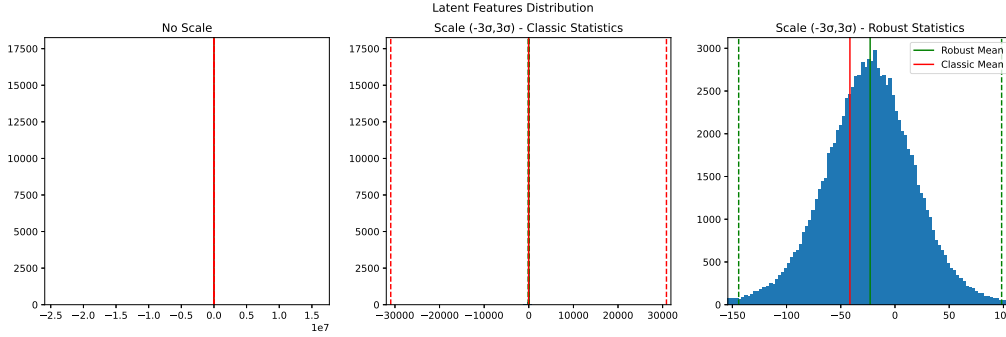


Figure 9: We present the latent feature distribution of a 3D *AutoDecoder* trained on MVImgNet[85]. The features are extracted at the 8^3 resolution, where we apply diffusion. The three subplots show different levels of “zooming in.” We see that the distribution spans a great range due to extreme outliers. Using classic mean and standard deviation computation, as we see in the middle subplot, still provides quite a large range of values. Normalizing the features using classic statistics leads to convergence failure for the diffusion model. We propose using robust statistics to normalize the distribution to $[-1, 1]$, before training the diffusion model. During inference, we de-normalize the diffusion output before feeding them to the upsampling layers of the autoencoder.

followed by a reshape operation to transform it into a 4^3 volume with 512 features per cell. This is followed by a series of four 3D residual blocks, each of which upsamples the volume resolution in each dimension and halves the features per cell, to a final resolution of 64^3 and 32 features.⁴ These blocks consist of two $3 \times 3 \times 3$ convolution blocks each followed by batch normalization in the main path, while the residual path consists of four $1 \times 1 \times 1$ convolutions, with ReLU applied after these operations. After the first of these blocks we have the 8^3 volume with 256 features per cell used for training our diffusion network, as in our final experiments. In this and the subsequent block, we apply self-attention layers [74] as described in Sec. 3.1. After the final upsampling block, we apply a final batch normalization followed by a $1 \times 1 \times 1$ convolution to produce the final $1 + 3$ density V^{Density} and RGB color features V^{RGB} used in our volumetric renderer.

Non-Rigid Architecture. For non-rigid subjects, our architecture produces $1 + 3 + 10$ output channels, with the latter group with the LBS weights for the $n_p = 10$ locally rigid components each region corresponds to in our canonical space. Our unsupervised 2D keypoint predictor uses the U-Net architecture of [62], which operates on a downsampled 64×64 input image to predict the locations of the keypoints corresponding to each of the 3D keypoints used to determine the pose of the camera relative to each region of the subject when it is aligned in the canonical volumetric space.

B.2 Latent 3D Diffusion

Diffusion Architecture and Sampling. For our base diffusion model architecture, we use the Ablated Diffusion Model (ADM) of Dhariwal *et al.* (2021) [15], a U-Net architecture originally designed for 2D image synthesis. We incorporate the preconditioning enhancements to this model described in Karras *et al.* (2022) [32]. As this architecture was originally designed for 2D, we adapt all convolutions and normalizations operations, as well as the attention mechanisms, to 3D.

For the cross-attention mechanism used for our conditioning experiments, we likewise extend the latent-space cross-attention mechanism from Rombach *et al.* (2022) [59] to our 3D latent space.

Robust Normalization. Autoencoder-based latent diffusion models impose a prior to the learned latent vector [59]. We find the latent features learned by our 3D autoencoder already form a bell-like curve. However, we also observe extreme values that can severely affect the calculation of the mean and standard deviation. As discussed in the main manuscript, we deploy the use of *robust normalization* to adjust the latent features. In particular, we take the *median* m as the center of the distribution and approximate its scale using the Normalized InterQuartile Range (IQR) [78] for a normal distribution: $0.7413 \times IQR$. We visualize its effect in Fig. 9. This is a crucial aspect of our approach, as in our experiments we find that without it, our diffusion training is unable to converge.

⁴We add one block to upsample to 128^3 for our aforementioned experiments with the ABO Tables dataset.



Figure 10: **Qualitative comparison of models trained at different latent resolutions.** All visualizations produced with 64 diffusion steps. We find that the model train on 8^3 latent features gives the best trade-off between quality and training speed, rendering it the best option for training on large-scale 3D datasets.

Ablating the latent volume resolution used for diffusion. We trained three diffusion models for the same time, resources, and number of parameters, for diffusion at 3 resolutions in our autoencoder: 4^3 , 8^3 , and 16^3 . We find that the 4^3 models, even when they train faster, often fail to converge to something meaning full and produce partial results. Most samples produced by the 16^3 models are of reasonable quality. However, many samples also exhibit spurious density values. We hypothesize that this is due to the model being under-trained. The 8^3 model produces the best results, and its fast training speed makes it suitable for large-scale training. We visualize the results in Fig. 10

B.3 Hash Embedding

Each object in the training set is encoded by an embedding vector. However, as we employ multi-view datasets of various scales, up to $\sim 300\text{K}$ unique targets from multiple categories, storing a separate embedding vector for each object depicted in the training images is burdensome⁵. As such, we experimented with a technique enabling the effective use of a significantly reduced number of embeddings (no more than $\sim 32\text{K}$ are required for any of our evaluations), while allowing effective content generation from large-scale datasets.

Similar to the approach in [51], we instead employ concatenations of smaller embedding vectors to create more combinations of unique embedding vectors used during training. For an embedding vector length l_v , the input embedding vector $H_k \in \mathbb{R}^{l_v}$ used for an object to be decoded is a concatenation of smaller embedding vectors h_i^j , where each vector is selected from an ordered codebook with n_c entries, with each entry containing collection of n_h embedding vectors of length l_v/n_c :

$$H_k = [h_1^{k_1}, h_2^{k_2}, \dots, h_{n_c}^{k_{n_c}}], \quad (9)$$

where $k_i \in \{1, 2, \dots, n_h\}$ is the set of indices used to select from the n_h possible codebook entries for position i in the final vector. This method allows for exponentially more combinations of embedding vectors to be provided during training than must be stored in learned embedding vector library.

However, while in [51], the index j for the vector h_i^j at position i is randomly selected for each position to access its corresponding codebook entry, we instead use a deterministic mapping from each training object index to its corresponding concatenated embedding vector. This function is implemented using a hashing function employing the multiplication method [14] for fast indexing using efficient bitwise operations. For object index k , the corresponding embedding index is:

$$m(k) = [(a \cdot k) \bmod 2^w] \gg (w - r), \quad (10)$$

⁵E.g., the codebook *alone* would require *six* times the parameters of the largest model in our experiments.

where the table has 2^r entries. w and a are heuristic hashing parameters used to reduce the number of collisions while maintaining an appropriate table size. We use 32 for w . a must be an odd integer between 2^{w-1} and 2^w [14]. We give each smaller codebook its own a value:

$$a_i = 2^{w-1} + 2 * i^2 + 1, \tag{11}$$

where i is the index of the codebook.

Discussion. In our experiments, we found that employing this approach had negligible impact on the overall speed and quality of our training and synthesis process. During training the memory of the GPU is predominantly occupied by the gradients, which are not affected by this hashing scheme. For Objaverse, our largest dataset using $\sim 300\text{K}$ images, using this technique saves approximately 800MB of GPU memory.

Interestingly, this also suggests that scaling this approach to larger datasets, should they become available, will require special handling. Learning this per-object embedding would soon become intractable. However, simply using this *hash embedding* approach reduces the model storage requirements by $\sim 75\%$ for this dataset.

In our experiments, we use hashing for ABO Tables, CelebV-Text and Objaverse, with codebook sizes $n_c =$ of 256, 8192 and 32768, respectively. We set the number of smaller codebooks (n_h) to 256 for each dataset.

C Implementation Details

C.1 Dataset Filtering

CelebV-Text [83]. Some heuristic filtering was necessary to obtain sufficient video quality and continuity for our purposes. We omit the first and last 10% of each video to remove fade-in/out effects, and any frames with less than 25% estimated foreground pixels. We also remove videos with less than 4 frames remaining after this, and any videos less than 200 kilobytes due to their relatively low quality. We also omit a small number of videos that were unavailable for download at the time of our experiments (the dataset is provided as a set of URLs for the video sources).

MVImgNet [85]. For these annotated video frames depicting real objects in unconstrained settings and environments, we applied Grounded Segment Anything [35] for background removal. However, as this process sometimes failed to produce acceptable segmentation results, we apply filtering to detect these cases. We first remove objects for which Grounding DINO [41] fails to detect bounding boxes. We then fit our volumetric autodecoder (Secs. 3.1-2) to only the *masks* produced by this segmentation (as monochrome images with a white foreground and a black background). For objects that are properly segmented in each frame, this produces a reasonable approximation of the object’s shape that is consistent in each of the input frames, while objects with incorrect or inconsistent segmentation will not be fit properly to the input images. Thus, objects for which the fitting loss is unusually high are removed.

Objaverse [12]. While Objaverse contains $\sim 800\text{K}$ 3D models, we found that the overall quality of these varied greatly, making many of them unsuitable for multi-view rendering. We thus filtered models without texture, material maps, or other color and appearance properties suitable, as well as models with an insufficient polygon count for realistic rendering. Interestingly, given the simplicity of the objects when rendered against a monochrome background, we found that the foreground segmentation supervision used for the other experiments described in Sec. 3.2 of the main paper was unnecessary. Given the scale of this dataset ($\sim 300\text{K}$ unique objects, with 6 frames per object), we thus omit this loss from our training process for this dataset for our final experiments for the sake of improved training efficiency. For datasets with more complex motion and real backgrounds, such as the real image datasets mentioned above, we found this supervision to be essential, as shown in Sec. A.2 and Fig. 6.

C.2 Additional Details

Training Details. Our experiments are implemented in the PyTorch [54, 55], using the PyTorch Lightning [17] framework for fast automatic differentiation and scalable GPU-accelerated

parallelization. For calculating the perceptual metrics (FID and KID), we used the Torch Fidelity [52] library.

We run our experiments on 8 NVIDIA A100 40GB GPUs per node. For some experiments, we use a single node, while for larger-scale experiments, we use up to 8 nodes in parallel.

We use the Adam optimizer [33] to train both the autoencoder and the diffusion Model. For the first network, we use a learning rate $lr = 5e - 4$ and beta parameters $\beta = (0.5, 0.999)$. For diffusion, we set the learning rate to $lr = 4.5e - 4$. We apply linear decay to the learning rate.

	<i>ABO-Tables</i>	<i>Chairs</i>	<i>CelebV-Text</i>	<i>MVImgNet</i>	<i>Objaverse</i>
<i>3D AutoDecoder</i>					
<i>z</i> -length	1024	1024	1024	1024	1024
MaxChannels	512	512	512	512	512
Depth	2	4	2	4	4
SA-Resolutions	8,16	8,16	8,16	8,16	8,16
ForegroundLoss λ	10	10	10	10	0
#Renders/batch	4	4	4	4	4
VoxelGridSize	$128^3 \times 4$	$64^3 \times 4$	$64^3 \times 14$	$64^3 \times 4$	$64^3 \times 4$
Learning Rate	5e-4	5e-4	5e-4	5e-4	5e-4
<i>Latent 3D Diffusion Model</i>					
<i>z</i> -shape	$8^3 \times 256$	$8^3 \times 256$	$8^3 \times 256$	$8^3 \times 256$	$8^3 \times 256$
Sampler	edm	edm	edm	edm	edm
Channels	128	128	192	192	192
Depth	2	2	3	3	3
Channel Multiplier	3,4	3,4	3,4	3,4	3,4
SA-resolutions	8,4	8,4	8,4	8,4	8,4
Learning Rate	4.5e-5	4.5e-5	4.5e-5	4.5e-5	4.5e-5
Conditioning	None	None	None/CA	None/CA	None/CA
CA-resolutions	-	-	8,4	8,4	8,4
Embedding Dimension	-	-	1024	1024	1024
Transformers Depth	-	-	1	1	2

Table 5: Architecture details for our models for each dataset. *SA* and *CA* stand for *Self-Attention* and *Cross-Attention* respectively. *z* refers to our 1D embedding vector and our latent 3D volume for the autoencoder and diffusion models, respectively. Note that for CelebV-Text, the output volume has 14 channels per cell: 3 for color values, 1 for density and 10 for part assignment.

Preparing the Text Embeddings for Text-Driven Generation. We train our model for text-conditioned image generation on three datasets: CelebV-Text [83], MVImgNet [85] and Objaverse [12]. The two latter datasets provide the object category of each sample, but they do not provide text descriptions. Using MiniGPT4 [87], we extract a description by providing a *hint* and the first view of each object along with the question: “<ImageHere> Describe this <hint> in one sentence. Describe its shape and color. Be concise, use only a single sentence.” For MVImgNet, this hint is the “class name”, while it is the “asset name” for Objaverse.

With the text-image pairs for these three datasets, we use the 11-billion parameter T5 [57] model to extract a sequence of text-embedding vectors. The dimensionality of these vectors is 1024. During training, we fix the length of the embedding sequence to 32 elements. We trim longer sentences and pad smaller sentences with zeroes.